ADVANCED ENERGY MATERIALS
www.advenergymat.de

High-Efficiency Inverted Polymer Photovoltaics via Spectrally Tuned Absorption Enhancement

Stephen Loser, Brent Valle, Kyle A. Luck, Charles K. Song, Gabriel Ogien, Mark C. Hersam, Kenneth D. Singer, and Tobin J. Marks**

Polymer photovoltaics represent one of several advancing technologies to fill the need for renewable energy sources in replacing current carbon-based energy production. Desirable mechanical properties, low-cost manufacturing, and straightforward customization through chemical synthesis have spurred rapid innovation and impressive efficiency increases.[1–6] However, further improvements in efficiency and stability are needed for commercial viability and widespread market adoption.[7] Two of the primary challenges being addressed to raise power conversion efficiency (PCE) are to synthesize new materials with reduced energetic loss between the optical bandgap and the open circuit voltage, while red-shifting absorption to capture a larger fraction of incident light,[8] and to maximize light absorption while overcoming an exciton diffusion length much shorter than the extinction length of the light.[9] The first challenge has been addressed largely by synthesizing conjugated molecular and polymeric donor materials with smaller optical band gaps.[10–12] This strategy has yielded donors that achieve confirmed PCEs on the order of 9%, with absorption extending throughout most of the visible spectrum. Regarding the second challenge, there are many means by which light absorption can be increased despite short exciton diffusion lengths. One of the most successful has been the implementation of the bulk-heterojunction (BHJ) architecture, which provides a large interfacial area for charge dissociation throughout the bulk of a relatively thick absorbing photoactive layer.[13–15]

In addition to, or as a complement to, the chemical synthesis of ever more efficient donors, the light absorption in the photoactive layer(s) can also be optimized by variation of the optical cavity properties of the photovoltaic device structure. For example, by systematically varying the thickness of the photoactive region (a tedious process), optical cavity modes that serve to enhance absorption can be tuned in frequency.[16] Furthermore, as we show here, optical transfer matrix simulations can be used to expeditiously optimize photocurrent generation in the photoactive region by shaping its absorption spectrum. In this contribution, transfer matrix calculations are shown to effectively guide OPV performance enhancement by spectral tuning in inverted polymer photovoltaic architectures.

Since both donor and acceptor materials in the active layer contact both electrodes in BHJ cells, interfacial layers (IFLs) are typically introduced to minimize leakage currents.[17] In conventional OPV device architectures, where holes are collected at the transparent indium tin oxide (ITO) anode and electrons at the reflective metal cathode, the archetypical IFL deposited on the ITO is the hole transport layer poly(3,4-ethylenedioxylenethiophene):poly(styrenesulphonic acid) (PEDOT:PSS). However, this layer limits device lifetime since it is corrosive,[18] hygroscopic,[19] and thermally unstable,[20] motivating alternative IFL materials strategies. Thus, an inverted device architecture (**Figure 1**), where ITO collects electrons and a high work function metal electrode collects holes, has proven very effective in enhancing both OPV performance and durability.[21,22] In the present work, an electron transport layer (ETL) coating is deposited on the ITO cathode. Solution deposited zinc oxide (ZnO) is a particularly effective ETL in inverted OPVs due to its large bandgap,[23] high electron mobility,[24] solar transparency,[25] and well-positioned conduction band energy for use with electron acceptors, such as fullerene derivatives.[26] While recent literature has demonstrated higher PCEs using a polymeric ETL in the inverted OPV architecture,[27] sol-gel ZnO is inexpensive, environmentally friendly,[28] and a common ETL in inverted OPVs, motivating this study on its impact in optical cavity strategies.[29] In addition to its favorable ETL properties, ZnO has also been used as an optical spacer[30] when adjacent to the reflective metal electrode, improving the distribution of optical intensity in conventional OPVs. In contrast, this work describes the very significant consequences for the optical intensity distribution of placing a ZnO layer adjacent to the transparent electrode in inverted architecture OPVs.

The inverted device architecture in this work utilizes a ZnO ETL and a BHJ active layer composed of the donor poly[[4,8-bis[(2-ethylhexyl)oxy]benzo[1,2-b:4,5-b′]dithiophene-2,6-diyl] [3-fluoro-2-[(2-ethylhexyl)carbonyl] thieno[3,4-b]thiophenediyl]] (PTB7) and the acceptor [6,6]-phenyl C_{71} butyric acid methyl-ester ($PC_{71}BM$; Figure 1). The PTB7:$PC_{71}BM$ active layer has been previously shown to yield large internal quantum efficiencies and exhibit absorption across much of the visible spectrum.[31,32] Furthermore, this active layer

S. Loser, C. K. Song, G. Ogien,
Prof. M. C. Hersam, Prof. T. J. Marks
Department of Chemistry and
the Argonne-Northwestern
Solar Energy Research (ANSER) Center
Northwestern University
2145 Sheridan Road
Evanston, IL 60208, USA
E-mail: t-marks@northwestern.edu
Dr. B. Valle, Prof. K. D. Singer
Department of Physics
Case Western Reserve University
10900 Euclid Avenue
Cleveland, OH 44106, USA
E-mail: kenneth.singer@case.edu
K. A. Luck, Prof. M. C. Hersam, Prof. T. J. Marks
Department of Materials Science and Engineering
Northwestern University
2200 Campus Drive
Evanston, IL 60208, USA

DOI: 10.1002/aenm.201301938

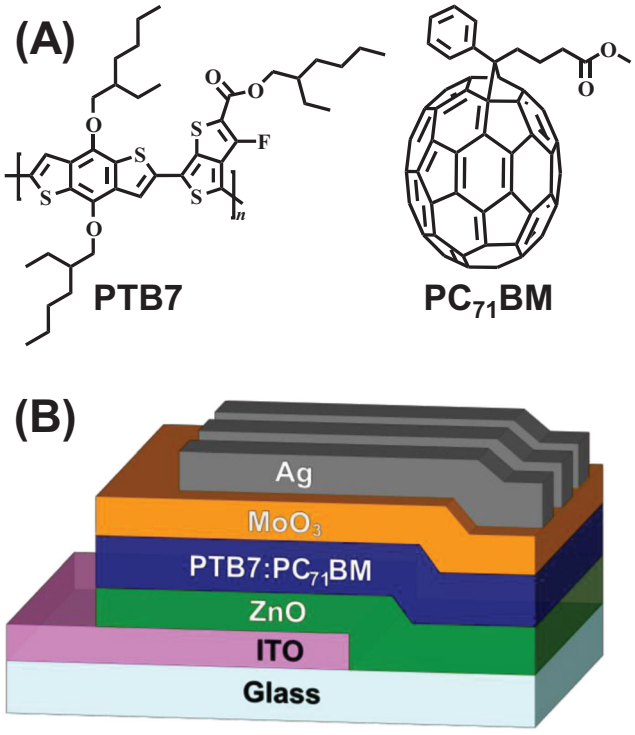

Figure 1. A) Chemical structures of the polymeric donor, PTB7, and acceptor, $PC_{71}BM$, comprising the OPV active layer used in this study. B) Diagram illustrating the inverted OPV architecture used here: glass (≈1 mm)/ITO (270 nm)/ZnO (thickness varied)/PTB7:$PC_{71}BM$ (thickness varied) /MoO_3 (10 nm)/Ag (100 nm).

system has achieved high PCE values of 7.5% in conventional OPV cells employing PEDOT:PSS,[31] 8.4% in inverted cells employing ZnO as the ETL,[33] and 8.6% with fluorophthalocyanine nanowire ZnO functionalization.[34] Note, however, that even in the case of BHJ microstructures, increasing the active layer thickness to enhance light harvesting becomes disadvantageous due to the modest charge carrier mobilities,[35] competing charge recombination processes,[36] and high trap state densities.[37] These limitations have fueled interest in additional or alternative means of light absorption enhancement, including using textures,[38,39] photonic crystals and diffractive elements,[40,41] plasmonic enhancement,[42,43] and optical interference effects.[44–47] In the present study, a strategy for the spectral tuning of absorption, validated by experimental results, is described, and optical transfer matrix theory[48–50] is used to efficiently guide OPV device design by optimizing the thickness of both the BHJ and the ETL layers. By tuning device layer thicknesses, we demonstrate that a range of absorption spectra are achievable and exploit cavity effects to spectrally sculpt absorption enhancement.[16] Furthermore, we compare external quantum efficiency (EQE) measurements and transfer matrix simulations to demonstrate the good agreement between theory and the experimental response of fabricated OPV devices. Finally, X-ray photoelectron spectroscopy (XPS), ultraviolet photoelectron spectroscopy (UPS), and atomic force microscopy (AFM) are used determine whether ZnO IFL thickness variations in any way affect charge generation and collection, beyond cavity effects.

Using optical transfer matrix theory, the total number of absorbed solar photons over the entire absorption spectrum and within the active layer versus the thicknesses of the active and ZnO layers is computed. The results are displayed as a contour in **Figure 2**A. Note that photon absorption increases within the active layer as the ZnO layer thickness decreases, indicating that, all other factors being equal, thinner ZnO layers are preferred optically in inverted OPVs, and that near an active layer thickness of 100 nm, more photons are absorbed than in 125 nm thick layers. The reason for this is illustrated more clearly in Figure 2B, where the calculation predicts that between 550 and 700 nm wavelengths, active layer thicknesses of ≈100 nm possess a region of enhanced absorption. A similar absorption enhancement repeats near a 250 nm active layer thickness. A frequency-pulling model described previously[16] explains the diagonal features of the enhanced absorption of the contour in Figure 2B. These calculated diagonal features appear as absorption maxima that shift in frequency as the active layer thickness is increased.

Transfer matrix simulations were next used to determine the optical field distribution within the OPV devices (see Figure 2C,D). For a device with a 100 nm PTB7:$PC_{71}BM$ active layer thickness, a single maximum of the optical field across most of the visible spectrum fits within the absorbing layer. This optical field distribution indicates concentration of light within the active layer and corresponds to the long-wavelength cavity enhancement observed in Figure 2B. Note however that for the 150 nm PTB7:$PC_{71}BM$ layer thickness, much of the active layer coincides with a minimum in the optical field. This minimum lowers the overall average optical energy density within the active region and results in reduced photovoltaic performance. With increased active layer thickness, more minima and maxima are brought into the active region, producing an oscillating average optical energy density within the active region as a function of PTB7:$PC_{71}BM$ layer thickness. This result also qualitatively explains why the amplitude of these oscillations diminishes with increased active layer thickness since the average optical energy density is increasingly less influenced by the addition of a new minimum or maximum in very thick devices.

Using the transfer matrix calculations as a guide, OPV devices were next fabricated as a function of ZnO layer and active layer thicknesses. As predicted by the calculations, the thinner the ZnO layer, the greater the device short-circuit current density (J_{SC}). In fact, for a 100 nm PTB7:$PC_{71}BM$ active layer thickness, the 3, 5, 18, 37, and 42 nm ZnO layers yield J_{SC} = 15.28, 15.01, 14.51, 14.21, and 13.93 mA cm^{-2}, respectively (**Figure 3**). Note, however, that while the transfer matrix calculations alone predict that a 0.0 nm ZnO layer should yield the highest J_{SC}, devices fabricated without the ZnO ETL fail to rectify and these results are not included in the summary of device metrics. Furthermore, as shown in Figure 3, the transfer matrix derived J_{SC} values scale well with active layer and ZnO thicknesses, as predicted. For the active layer thicknesses investigated (40–100 nm), the measured J_{SC} values to some degree outperform the transfer matrix predictions. This additional absorption may be due to scattering within the device or to

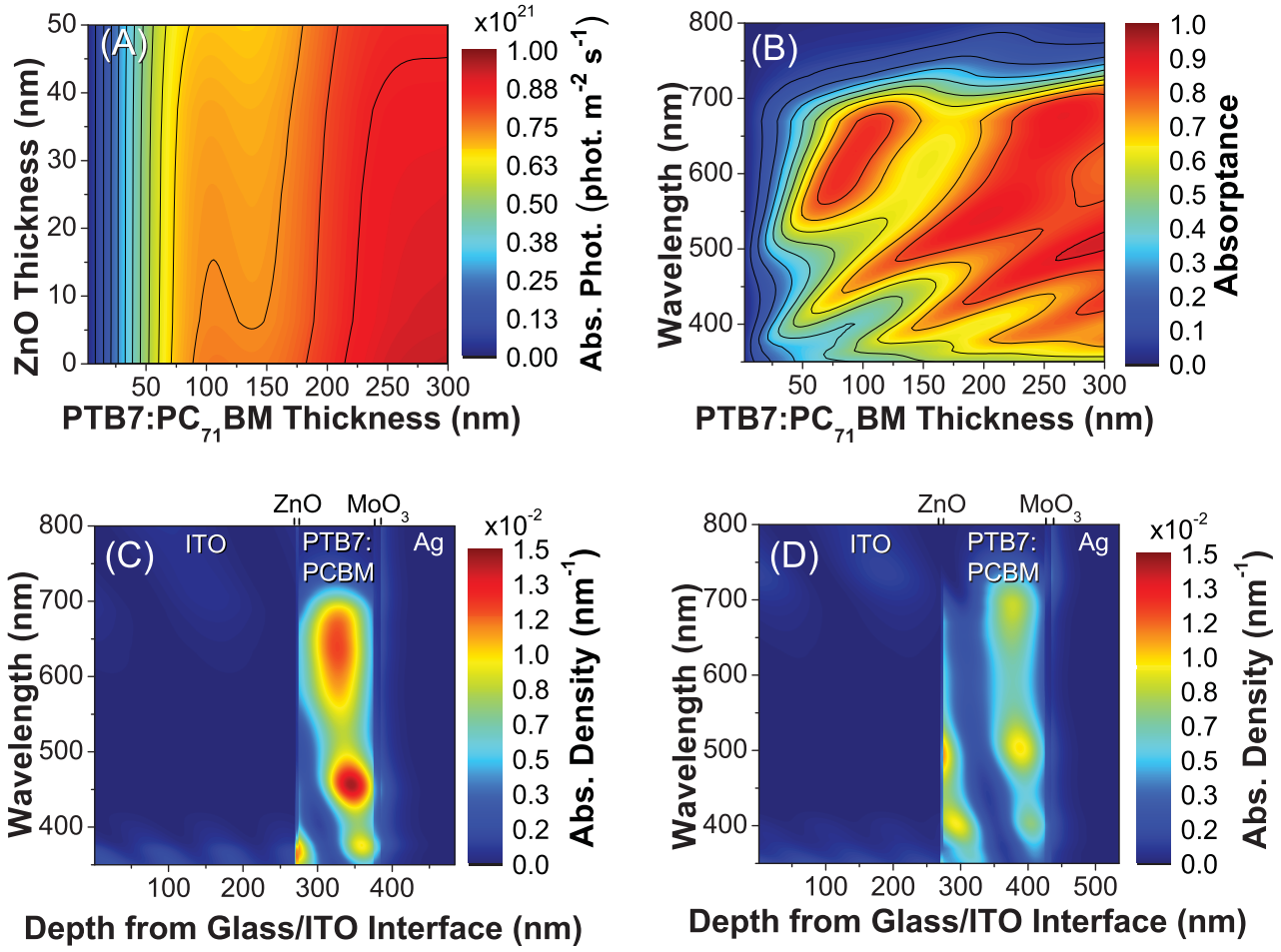

Figure 2. A) Contours depicting the transfer matrix simulated total solar absorbed photons as a function of the ZnO and active layer thicknesses. Over the range of thicknesses simulated, the number of absorbed photons increases as the ZnO thickness is decreased. As the active layer thickness is increased, the absorbed photons increase due to enhanced absorbance near 100 nm and 275 nm. B) A spectral absorbance contour versus active layer thickness for a sample with a 5 nm ZnO layer thickness illustrating cavity enhanced absorption effects that shift active layer absorbance spectra as the thickness is varied. C,D) Transfer matrix absorbance calculations within the OPV structures illustrating the positions and wavelengths at which absorption occurs. Both architectures simulated have ZnO thickness of 5 nm and active layer thicknesses of 100 nm (C) and 150 nm (D).

changes in optical parameters, which are not accounted for in these simulations. Table S1 (Supporting Information) summarizes the measured OPV performance metrics.

The decreased photocurrent for thick ZnO layers in the inverted structures observed here can be contrasted with optical spacer effects[30,51,52] where the same thin film optical

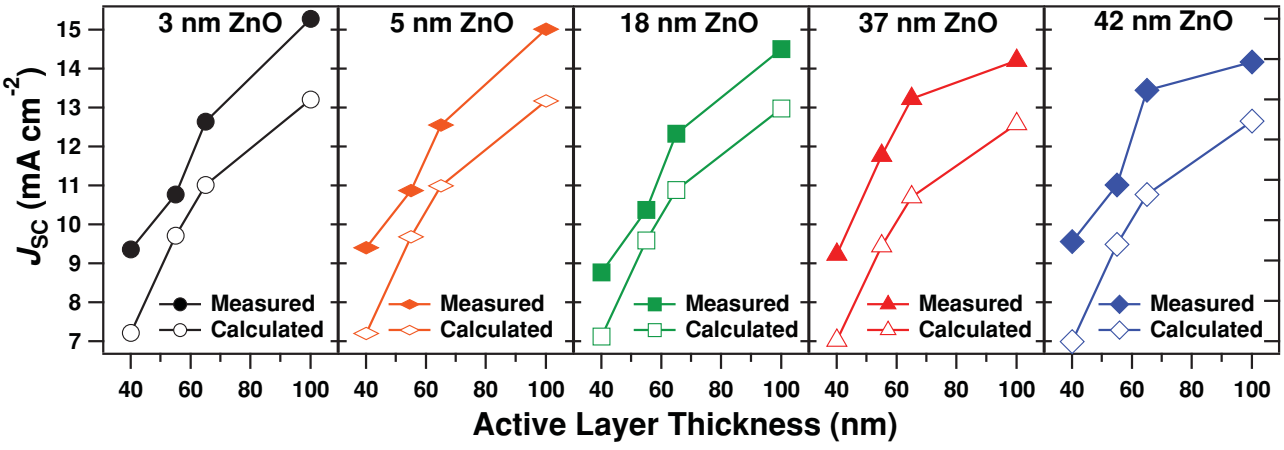

Figure 3. Comparison of measured and calculated J_{SC} as a function of ZnO and PTB7:PC_{71}BM layer thicknesses.

physics suggest a thick transparent charge transfer layer should be used. The effect of inserting an optical spacer adjacent to the highly-reflective cathode in a conventional OPV is to maintain a large optical field density in the BHJ region where the optical field has nearly completely decayed. Note, however, that in inverted OPVs, the ZnO IFL is proximate to the ITO electrode. Here this transparent "optical spacer" occupies valuable space in the weak optical cavity formed by the electrodes instead of occupying a decayed field region. Therefore, in inverted devices the thickness of this layer must be minimized so that the active layer fills as large a fraction of the optical cavity as possible.

The significance of the present cavity effects on OPV active layer absorption spectra and how they influence short-circuit current is important to emphasize. OPV performance is often characterized and optimized by empirically varying device architecture and layer thicknesses. However, optical modeling as discussed here provides critical information for the accurate and expeditious analysis of absorption, thereby differentiating optical interference effects from charge generation and collection effects. Importantly, the incorporation of total absorbed photons obtained by integrating over the entire absorption spectrum is needed to accurately access optical interference effects on overall device performance. Also, optical cavity absorption enhancements are a confounding factor in any analysis of thickness-dependent OPV performance features and cannot be ignored. For example, thickness-dependent morphology changes and their impact on device performance cannot be properly evaluated without first accounting for thickness-dependent optical cavity effects using transfer matrix methods.

To investigate if varying the ZnO IFL thickness impacts OPV performance via non-cavity mechanisms, XPS, UPS, and AFM imaging were employed. The XPS survey spectra (Figure S1, Supporting Information) confirm the presence of ZnO for every IFL thickness prepared, as evidenced by the observed Zn $3p^{3/2}$ and O 1s peak evolutions, arguing that each thickness has a similar ZnO composition. The UPS spectra (Figure S2, Supporting Information) reveal that the valence band (VB) energy shifts slightly from 7.53 to 7.82 eV as the ZnO thickness is increased from 3.0 to 42 nm. Accordingly, the CB energy, calculated by extrapolation using the optical band edge (Figure S3, Supporting Information) and the VB energy, decreases in magnitude by ≈0.44 eV, from 3.92 to 4.36 eV, as the ZnO film thickness is increased. This type of shift in VB energy is a common phenomenon originating from the rearrangement of charge density to equilibrate the Fermi level at interfaces.[53–56] Despite this effect, we observe minimal variation in both the device open circuit voltage (V_{OC}) and fill factor (*FF*) as a function of ZnO thickness (Table S1, Supporting Information). However, as Table S2 (Supporting Information) tabulates and Figure S5 (Supporting Information) shows graphically, J_{SC} decreases as the offset between the CB of ZnO and the lowest unoccupied molecular orbital (LUMO) of $PC_{71}BM$ increases, which is presumably caused by the larger Schottky barriers arising from the thicker ZnO layers.[57] In spite of the band shifts, we note that the transfer matrix modeling can be used to accurately predict the J_{SC} trend as a function of ZnO thickness. Finally, the AFM images (Figure S6, Supporting Information) reveal that all the ZnO films have similar morphologies, arguing that the structure of the ZnO/active layer interface remains essentially constant. These results strongly argue that the transfer matrix simulation alone suffices for selecting the optimal ZnO IFL thickness.

We next sought to investigate the influence of the PTB7:$PC_{71}BM$ active layer thickness on the PV performance in greater detail. Using a thin (5 nm) ZnO IFL, OPVs with active layer thicknesses between 40 and 300 nm were fabricated and characterized (**Figure 4** and **Table 1**). Note that even though the 3 nm ZnO layer affords somewhat greater J_{SC}s and high PCEs at lower active layer thicknesses, 5 nm was chosen because it yields a higher PCE for 100 nm active layers with less device performance variability (see Table S1, Supporting Information). As expected, both the measured and calculated J_{SC}s increase concomitantly with active layer thickness, and a very high J_{SC} of 16.70 mA cm^{-2} is achieved for a 250 nm PTB7:$PC_{71}BM$ active layer. However, due to the significantly depressed *FF* for the thickest active layers, presumably arising from trap-assisted recombination,[58–61] the high J_{SC} alone is insufficient to yield the largest PCEs. This decreased *FF* is the primary origin of the lower PCEs for the thickest devices, and the resulting plot of PCE vs active layer thickness reveals a maximum PCE near 100 nm (Figure 4C). Note also that the V_{OC} variation is small (≈40 mV) and does not depend greatly on the active layer thickness, despite the shifts in absorption spectra.

EQE measurements reveal the input wavelength dependence of the external device current, and in the present results reveal subtle changes in absorption due to optical cavity effects. Comparing absorbance within the active layer predicted by optical transfer matrix theory versus the experimental EQE data (**Figure 5**), which is equivalent to assuming an internal quantum efficiency of unity, yields good agreement, especially for thicker active layer devices. The optical maxima wavelengths that shift according to the optical simulations as the active layer thickness is increased, are seen to coincide with the maxima in the EQE spectra. This good agreement between simulated absorption within the active layer and the measured EQE spectra underscore the attraction of using optical transfer matrix theory to optimize and tune OPV absorption spectra. Furthermore, because many of the EQE spectral features result from optical cavity effects, transfer matrix simulations provide a critical computational complement to EQE measurements. Comparing differences between transfer matrix theory computed absorption and measured EQE spectra should provide important information about charge collection within the photoactive region.

In summary, optical transfer matrix modeling can be used productively to investigate and optimize absorption within the active layer of inverted PTB7:$PC_{71}BM$ solar cells. Using thin ZnO IFLs and active layer thicknesses as design parameters, total absorbed solar photons can be maximized to achieve optimal device performance. Two design guidelines emerge from the transfer matrix modeling and are then realized in physical devices: 1) the ZnO layer thickness should be minimized so that a maximum fraction of the weak optical cavity formed by reflective and transparent electrodes is composed of PTB7:$PC_{71}BM$. This result stands in contrast to the concept

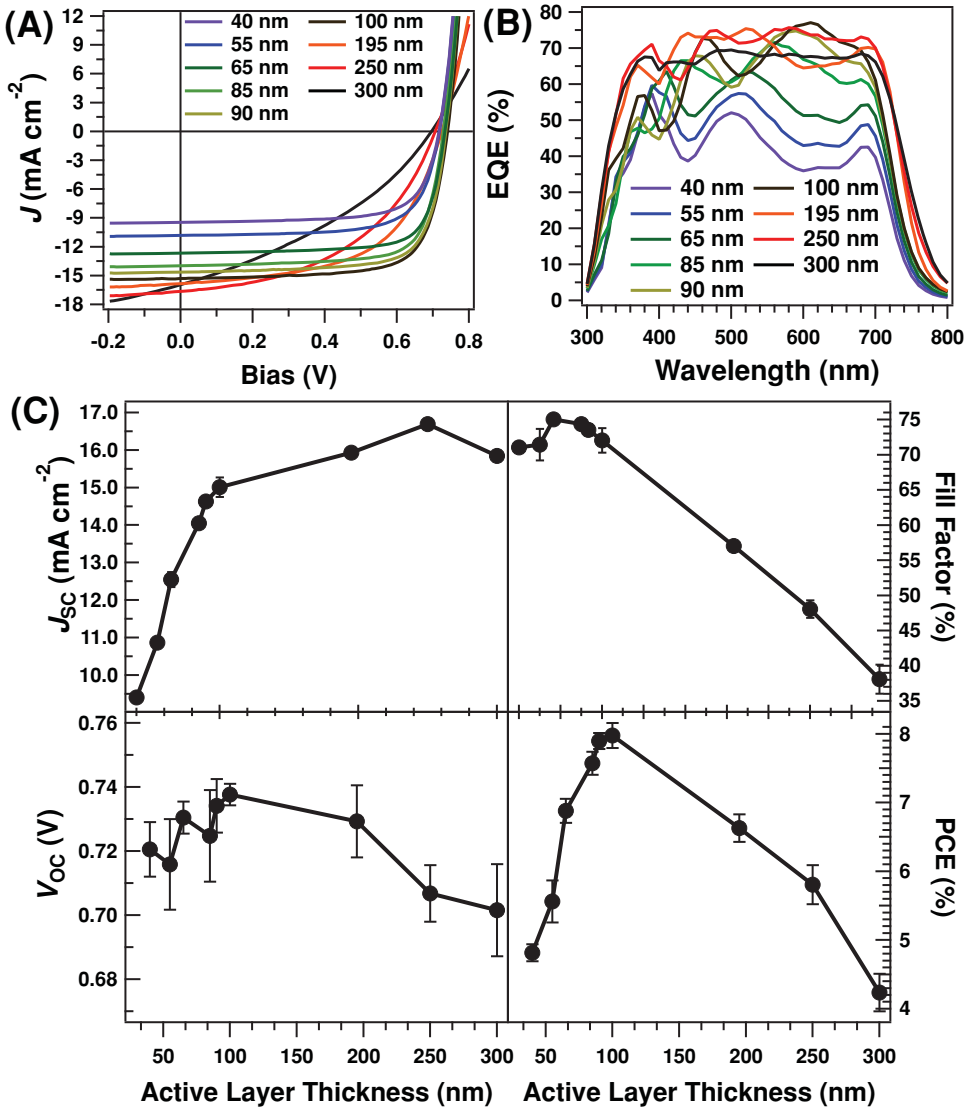

Figure 4. OPV response as a function of PTB7:$PC_{71}BM$ active layer thickness. A) Typical *J–V* response and B) EQE response for a 5 nm ZnO ETL. C) Short-circuit current density (upper left), fill factor (upper right), open circuit voltage (lower left), and power conversion efficiency (lower right), plotted versus the thickness of the PTB7:$PC_{71}BM$ active layer. Short circuit current density calculated from spectrally integrated EQE spectra is compared to short circuit current density calculated assuming 100% internal quantum efficiency. Large fill factors are observed for sub-100 nm active layer thicknesses, which then decrease as the thickness is increased. Despite shifts in active layer absorption spectra, including shifts of the absorption edge to longer wavelengths, open circuit voltage remains constant within experimental uncertainty. Power conversion efficiency exhibits a peak for 100 nm active layer thickness due to increasing short circuit current density versus thickness, and decreasing fill factor versus thickness beyond 100 nm.

of an "optical spacer" adjacent to the reflective metal cathode advanced by others.[52] 2) A local maximum in total absorbed photons occurs at active layer thicknesses near 100 nm, and this local maximum is optimal for avoiding the recombination losses typical of much thicker devices. The optimal active layer thicknesses determined by transfer matrix calculations, and the corresponding active layer absorption spectra, provide predictive metrics that can be used to guide device architecture design, eliminating the need for inefficient empirical searches over a wide range of device thickness parameters. Optical design could also lead to new materials for efficient devices in ultrathin layers, circumventing the modest charge carrier mobilities typical of photoactive OPV materials and potentially eliminating the need for the bulk heterojunction.[62–64] Moreover, the good agreement between the experimental EQE data and transfer matrix calculations demonstrate how optical modeling enhances device design capabilities. The short-circuit currents, fill factors, and power conversion efficiencies achieved here in inverted PTB7:$PC_{71}BM$ devices validate this approach.

Experimental Section

ZnO Precursor Preparation and OPV Fabrication: The inverted solar cells fabricated in this study have the structure: glass/ITO/ZnO/

Table 1. Glass/ITO/5 nm ZnO/PTB7:$PC_{71}BM$/MoO_3/Ag OPV *J–V* response as a function of active layer thickness. Average measurements with standard deviation in parenthesis. Average based on 16 devices.

Active layer thickness [nm]	V_{OC} [V]	*FF* [%]	J_{SC}, calculated[a)] [mA cm^{-2}]	J_{SC}, measured [mA cm^{-2}]	*PCE* [%]
40	0.721 (±0.008)	71.1 (±0.6)	7.20	9.40 (±0.09)	4.82 (±0.13)
55	0.716 (±0.014)	71.5 (±2.3)	9.68	10.87 (±0.08)	5.56 (±0.30)
65	0.730 (±0.005)	75.0 (±0.4)	10.99	12.55 (±0.20)	6.88 (±0.17)
85	0.725 (±0.014)	74.4 (±0.5)	12.65	14.05 (±0.05)	7.57 (±0.17)
90	0.734 (±0.008)	73.5 (±0.8)	12.88	14.63 (±0.10)	7.90 (±0.12)
100	0.738 (±0.003)	72.0 (±1.7)	13.17	15.01 (±0.26)	7.98 (±0.18)
195	0.729 (±0.011)	57.0 (±0.6)	14.66	15.94 (±0.13)	6.63 (±0.20)
250	0.707 (±0.009)	48.1 (±1.2)	16.13	16.70 (±0.05)	5.81 (±0.29)
300	0.702 (±0.014)	38.1 (±2.1)	16.46	15.84 (±0.10)	4.23 (±0.27)

a) Calculated J_{SC} based on TM modeling.

PTB7:$PC_{71}BM$/MoO_3/Ag (Figure 1b). Transfer matrix calculations guided design of the range of the layer thicknesses used and are described below. Patterned ITO-coated glass substrates were obtained from Thin Film Devices, Inc. ITO substrates (270 nm, <10 Ω/sq.) were cleaned by progressive sonications in aqueous detergent, DI water, methanol, isopropanol, and acetone, followed by a 20 min UV-ozone treatment at 150 °C. Various thicknesses of ZnO layers were deposited on the clean substrates by spin-coating from solutions with a range of molar concentrations. A stock 0.50 M Zn-precursor solution was prepared by adding 329.4 mg $Zn(CH_3COO)_2{\cdot}2H_2O$ (99.99%, Sigma-Aldrich) to 3 mL 2-methoxyethanol (anhydrous, Sigma-Aldrich) in 90 µL ethanolamine (distilled, Sigma-Aldrich). This solution was aged 24 h to ensure complete dissolution. Then, 0.25 M, 0.10 M, and 0.050 M solutions were prepared by diluting the 0.50 M stock solution appropriately with 2-methoxyethanol. The 0.50 M ZnO layer was spun-cast at either 2000 RPM or 4000 RPM for 40 s to afford 42 or 37 nm films, respectively. The 0.25 M, 0.10 M, and 0.050 M solutions were all spun at 4000 RPM for 40 s to afford 18, 5, and 3 nm films, respectively. All films were then baked under air at 170 °C for 10 min and then transferred to a N_2-filled glovebox. Solutions of PTB7:$PC_{71}BM$ (1.0:1.5 wt) at a concentration of 10 mg mL^{-1} were prepared in chlorobenzene with the processing additive 1,8-diiodoctane (97:3% vol). Thickness of the deposited active layer was varied via the speed and acceleration during spin-coating. Finally, the MoO_3 IFL (10 nm) and Ag (100 nm) anode were deposited by thermal evaporation through a shadow mask to give a defined active area of 0.07 cm^2. The active layer solution preparation and all subsequent fabrication were performed under a N_2 atmosphere. All layer thicknesses were measured using a Veeco Dektak 150 stylus profilometer.

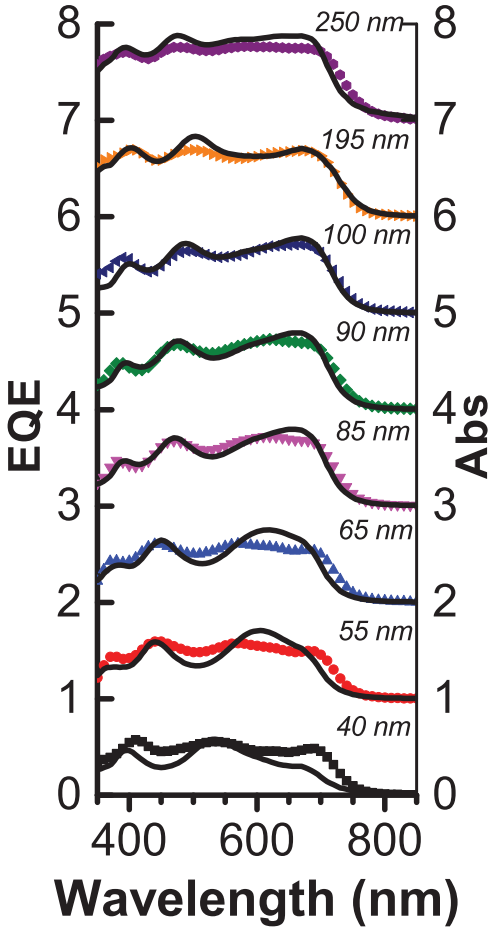

Figure 5. Comparison of experimental OPV EQE data (colored points) and transfer matrix calculated active layer absorbance spectra (black solid curves) for various PTB7:$PC_{71}BM$ active layer thicknesses (250–40 nm) with a 5 nm ZnO ETL. Traces are offset for clarity.

OPV Characterization: *J–V* curves of all devices were measured with a Keithley 2400 source meter and an Oriel Sol2A solar simulator (AM1.5G, 100 mW cm^{-2}) integrated into a N_2-filled glovebox. Spectrally resolved EQEs were measured using a benchtop QEX10 measurement system supplied by PV Measurements Inc.

Absorption and Ellipsometry Measurements: Optical absorption calculations within each layer of the device were performed using optical transfer matrix theory in the wavelength range 350–900 nm. Complex refractive index spectra for the materials used were determined using variable angle spectroscopic ellipsometry (Uvisel DUV-NIR, Horiba).

XPS, UPS, and AFM: The XPS and UPS spectra were recorded on a Thermo Scientific ESCALAB 250Xi system, at a base pressure of 8×10^{-10} mbar (UHV), using a monochromated Al Kα X-ray source at $h\nu = 1486$ eV. The UPS data were collected with a 21.2 eV He(1) source at a pass energy of 2.0 eV and an energy step size of 0.05 eV. The instrument was calibrated with gold foil and a –10 V sample bias was applied to determine the secondary electron cut off (SECO) for all samples by curve fitting. Three measurements were averaged for each sample. AFM data were recorded using silicon cantilevers (Applied NanoStructures, Inc.) on a Veeco Dimension ICON PT AFM System in tapping mode.

Supporting Information

Supporting Information is available from the Wiley Online Library or from the author.

Acknowledgements

S.L. and B.V. contributed equally to this work. This research was supported by the NSF STC program through the Center for Layered Polymer Systems (CLiPS; grant DMR-0423914;S.L., B.V., OPV fabrication and modeling), by the U.S. Department of Energy (grant DE-0000275; C.K.S., OPV characterization), and by the ANSER Center, an Frontier Research Center funded by the U.S. Department of Energy, Office of Science, Office of Basic Energy Sciences under Award Number DE-SC0001059 (K.A.L., OPV characterization). The authors acknowledge the contribution of the State of Ohio, Department of Development, Third Frontier Commission, which provided funding in support of the Research Cluster on Surfaces in Advanced Materials. The XPS, UPS, and AFM studies were performed at the KECK-II, EPIC, and NIFTI facilities of the NUANCE Center at Northwestern University, which is supported by NSF-NSEC, NSF-MRSEC (DMR-1121262), the Keck Foundation, the State of Illinois, and Northwestern University. K.A.L. acknowledges a graduate fellowship through the NSF Graduate Research Fellowship Program.

Received: December 17, 2013
Revised: April 20, 2014
Published online: May 19, 2014

[1] M. Graetzel, R. A. J. Janssen, D. B. Mitzi, E. H. Sargent, *Nature* **2012**, *488*, 304.
[2] X. Guo, N. Zhou, S. J. Lou, J. Smith, D. B. Tice, J. W. Hennek, R. P. Ortiz, J. T. L. Navarrete, S. Li, J. Strzalka, L. X. Chen, R. P. H. Chang, A. Facchetti, T. J. Marks, *Nat. Photonics* **2013**, *7*, 825.
[3] D. Ginley, M. A. Green, R. Collins, *MRS Bull.* **2008**, *33*, 355.
[4] A. C. Mayer, S. R. Scully, B. E. Hardin, M. W. Rowell, M. D. McGehee, *Mater. Today* **2007**, *10*, 28.
[5] H. Spanggaard, F. C. Krebs, *Sol. Energy Mater. Sol. Cells* **2004**, *83*, 125.
[6] S. R. Forrest, *Nature* **2004**, *428*, 911.
[7] C. J. Brabec, J. A. Hauch, P. Schilinsky, C. Waldauf, *MRS Bull.* **2005**, *30*, 50.
[8] E. T. Hoke, K. Vandewal, J. A. Bartelt, W. R. Mateker, J. D. Douglas, R. Noriega, K. R. Graham, J. M. J. Frechet, A. Salleo, M. D. McGehee, *Adv. Energy Mater.* **2013**, *3*, 220.
[9] S. R. Forrest, *MRS Bull.* **2005**, *30*, 28.
[10] W. W. Li, K. H. Hendriks, W. S. C. Roelofs, Y. Kim, M. M. Wienk, R. A. J. Janssen, *Adv. Mater.* **2013**, *25*, 3182.
[11] Z. B. Henson, G. C. Welch, T. van der Poll, G. C. Bazan, *J. Am. Chem. Soc.* **2012**, *134*, 3766.
[12] P.-L. T. Boudreault, A. Najari, M. Leclerc, *Chem. Mater.* **2011**, *23*, 456.
[13] Y. Y. Liang, Z. Xu, J. B. Xia, S. T. Tsai, Y. Wu, G. Li, C. Ray, L. P. Yu, *Adv. Mater.* **2010**, *22*, E135.
[14] G. Li, V. Shrotriya, J. S. Huang, Y. Yao, T. Moriarty, K. Emery, Y. Yang, *Nat. Mater.* **2005**, *4*, 864.
[15] G. Yu, J. Gao, J. C. Hummelen, F. Wudl, A. J. Heeger, *Science* **1995**, *270*, 1789.
[16] B. Valle, S. Loser, J. W. Hennek, V. DeGeorge, C. Klosterman, J. H. Andrews, K. D. Singer, T. J. Marks, *Opt. Express* **2012**, *20*, A954.
[17] J. D. Servaites, M. A. Ratner, T. J. Marks, *Energy Environ. Sci.* **2011**, *4*, 4410.
[18] Y. Suh, N. Lu, S. H. Lee, W. S. Chung, K. Kim, B. Kim, M. J. Ko, M. J. Kim, *ACS Appl. Mater. Interfaces* **2012**, *4*, 5118.
[19] H. S. Kang, H. S. Kang, J. K. Lee, J. W. Lee, J. Joo, J. M. Ko, M. S. Kim, J. Y. Lee, *Synth. Met.* **2005**, *155*, 176.
[20] E. Vitoratos, S. Sakkopoulos, E. Dalas, N. Paliatsas, D. Karageorgopoulos, F. Petraki, S. Kennou, S. A. Choulis, *Org. Electron.* **2009**, *10*, 61.
[21] Y. Sun, J. H. Seo, C. J. Takacs, J. Seifter, A. J. Heeger, *Adv. Mater.* **2011**, *23*, 1679.
[22] L.-M. Chen, Z. Hong, G. Li, Y. Yang, *Adv. Mater.* **2009**, *21*, 1434.
[23] M. S. White, D. C. Olson, S. E. Shaheen, N. Kopidakis, D. S. Ginley, *Appl. Phys. Lett.* **2006**, *89*, 143517.
[24] S. K. Hau, H. L. Yip, N. S. Baek, J. Y. Zou, K. O'Malley, A. K. Y. Jen, *Appl. Phys. Lett.* **2008**, *92*, 253301.
[25] M. Berber, V. Bulto, R. Kliss, H. Hahn, *Scripta Mater.* **2005**, *53*, 547.
[26] H. L. Yip, A. K. Y. Jen, *Energy Environ. Sci.* **2012**, *5*, 5994.
[27] Z. He, C. Zhong, S. Su, M. Xu, H. Wu, Y. Cao, *Nat. Photonics* **2012**, *6*, 591.
[28] W. J. E. Beek, M. M. Wienk, R. A. J. Janssen, *Adv. Mater.* **2004**, *16*, 1009.
[29] L. Dou, J. You, Z. Hong, Z. Xu, G. Li, R. A. Street, Y. Yang, *Adv. Mater.* **2013**, *25*, 6642.
[30] A. K. Kyaw, D. H. Wang, D. Wynands, J. Zhang, T. Q. Nguyen, G. C. Bazan, A. J. Heeger, *Nano Lett.* **2013**, *13*, 3796.
[31] Y. Liang, Z. Xu, J. Xia, S.-T. Tsai, Y. Wu, G. Li, C. Ray, L. Yu, *Adv. Mater.* **2010**, *22*, E135.
[32] H.-Y. Chen, J. Hou, S. Zhang, Y. Liang, G. Yang, Y. Yang, L. Yu, Y. Wu, G. Li, *Nat. Photonics* **2009**, *3*, 649.
[33] F.-L. Kuo, Y. Li, M. Solomon, J. Du, N. D. Shepherd, *J. Phys. D: Appl. Phys.* **2012**, *45*, 065301.
[34] S. M. Yoon, S. J. Lou, S. Loser, J. Smith, L. X. Chen, A. Facchetti, T. J. Marks, *Nano Lett.* **2012**, *12*, 6315.
[35] T. Kirchartz, T. Agostinelli, M. Campoy-Quiles, W. Gong, J. Nelson, *J. Phys. Chem. Lett.* **2012**, *3*, 3470.
[36] M. Lenes, L. J. A. Koster, V. D. Mihailetchi, P. W. M. Blom, *Appl. Phys. Lett.* **2006**, *88*, 243502.
[37] Z. M. Beiley, E. T. Hoke, R. Noriega, J. Dacuna, G. F. Burkhard, J. A. Bartelt, A. Salleo, M. F. Toney, M. D. McGehee, *Adv. Energy Mater.* **2011**, *1*, 954.
[38] J. Li, L. Zuo, H. Pan, H. Jiang, T. Liang, Y. Shi, H. Chen, M. Xu, *J. Mater. Chem. A* **2013**, *1*, 2379.
[39] L. Muller-Meskamp, Y. H. Kim, T. Roch, S. Hofmann, R. Scholz, S. Eckardt, K. Leo, A. F. Lasagni, *Adv. Mater.* **2012**, *24*, 906.
[40] D. H. Ko, J. R. Turnbleston, W. Schenck, R. Lopez, E. T. Samulski, *J. Phys. Chem. C* **2011**, *115*, 4247.
[41] J. R. Tumbleston, D. H. Ko, E. T. Samulski, R. Lopez, *Opt. Express* **2009**, *17*, 7670.
[42] Q. Q. Gan, F. J. Bartoli, Z. H. Kafafi, *Adv. Mater.* **2013**, *25*, 2385.
[43] H. A. Atwater, A. Polman, *Nat. Mater.* **2010**, *9*, 205.
[44] N. P. Sergeant, B. Niesen, A. S. Liu, L. Boman, C. Stoessel, P. Heremans, P. Peumans, B. P. Rand, S. H. Fan, *Opt. Lett.* **2013**, *38*, 1431.
[45] N. P. Sergeant, A. Hadipour, B. Niesen, D. Cheyns, P. Heremans, P. Peumans, B. P. Rand, *Adv. Mater.* **2012**, *24*, 728.
[46] M. Agrawal, P. Peumans, *Opt. Express* **2008**, *16*, 5385.
[47] A. J. Moulé, K. Meerholz, *Appl. Phys. B* **2007**, *86*, 721.
[48] Y. Long, *Sol. Energy Mater. Sol Cells* **2010**, *94*, 744.
[49] D. W. Sievers, V. Shrotriya, Y. Yang, *J. Appl. Phys.* **2006**, *100*, 114509.
[50] L. A. A. Pettersson, L. S. Roman, O. Inganas, *J. Appl. Phys.* **1999**, *86*, 487.
[51] T. Ameri, G. Dennler, C. Waldauf, P. Denk, K. Forberich, M. C. Scharber, C. J. Brabec, K. Hingerl, *J. Appl. Phys.* **2008**, *103*, 084506.

[52] J. Y. Kim, S. H. Kim, H. H. Lee, K. Lee, W. L. Ma, X. Gong, A. J. Heeger, *Adv. Mater.* **2006**, *18*, 572.
[53] Z. Zhang, J. T. Yates, *Chem. Rev.* **2012**, *112*, 5520.
[54] M. T. Greiner, L. Chai, M. G. Helander, W.-M. Tang, Z.-H. Lu, *Adv. Funct. Mater.* **2012**, *22*, 4557.
[55] P. G. Schroeder, C. B. France, J. B. Park, B. A. Parkinson, *J. Phys. Chem. B* **2003**, *107*, 2253.
[56] L. J. Brillson, *Surf. Sci.* **1994**, *299–300*, 909.
[57] H. Ishii, K. Sugiyama, E. Ito, K. Seki, *Adv. Mater.* **1999**, *11*, 605.
[58] L. M. Andersson, C. Muller, B. H. Badada, F. L. Zhang, U. Wurful, O. Inganas, *J. Appl. Phys.* **2011**, *110*, 024509.
[59] D. Gupta, S. Mukhopadhyay, K. S. Narayan, *Sol. Energy Mater. Sol. Cells* **2010**, *94*, 1309.
[60] S. R. Cowan, A. Roy, A. J. Heeger, *Phys. Rev. B* **2010**, *82*, 245207.
[61] R. A. Street, M. Schoendorf, A. Roy, J. H. Lee, *Phys. Rev. B* **2010**, *81*, 205307.
[62] H. Song, L. Guo, Z. Liu, X. Zeng, D. Ji, N. Zhang, H. Hu, S. Jiang, Q. Gan, *Adv. Mater.* **2014**, *26*, 2727.
[63] M. A. Kats, R. Blanchard, S. Ramanathan, F. Capasso, *Opt. Photonics News* **2014**, *25*, 40.
[64] M. A. Kats, R. Blanchard, P. Genevet, F. Capasso, *Nat. Mater.* **2013**, *12*, 20.